

Title	Reynolds number limits for jet propulsion: A numerical study of simplified jellyfish	
Corresponding Author	Family Name	Miller
	Given Name	Laura
	Division	Department of Mathematics
	Organization	University of North Carolina
	Address	27599-3250, Chapel Hill, NC, USA
	Email	lam9@email.unc.edu
Author	Family Name	Herschlag
	Given Name	Gregory
	Division	Department of Mathematics
	Organization	University of North Carolina
	Address	27599-3250, Chapel Hill, NC, USA
	Email	gregoryh@email.unc.edu

Abstract

The Scallop Theorem states that reciprocal methods of locomotion, such as jet propulsion or paddling, will not work in Stokes flow (Reynolds number = 0). In nature the effective limit of jet propulsion is still in the range where inertial forces are significant. It appears that almost all animals that use jet propulsion swim at Reynolds numbers (Re) of about 5 or more. Juvenile squid and octopods hatch from the egg already swimming in this inertial regime. Juvenile jellyfish, or ephyrae, break off from polyps swimming at Re greater than 5. Many other organisms, such as scallops, rarely swim at Re less than 100. The limitations of jet propulsion at intermediate Re is explored here using the immersed boundary method to solve the two-dimensional Navier Stokes equations coupled to the motion of a simplified jellyfish. The contraction and expansion kinematics are prescribed, but the forward and backward swimming motions of the idealized jellyfish are emergent properties determined by the resulting fluid dynamics. Simulations are performed for both an oblate bell shape using a paddling mode of swimming and a prolate bell shape using jet propulsion. Average forward velocities and work put into the system are calculated for Re between 1 and 320. The results show that forward velocities rapidly decay with decreasing Re for all bell shapes when $Re < 10$. Similarly, the work required to generate the pulsing motion increases significantly for $Re < 10$. When compared actual organisms, the swimming velocities and vortex separation patterns for the model prolate agree with those observed in *Nemopsis bachei*. The forward swimming velocities of the model oblate jellyfish after two pulse cycles are comparable to those reported for *Aurelia aurita*, but discrepancies are observed in the vortex dynamics between when the 2D model oblate jellyfish and the organism. This discrepancy is likely due to a combination of the differences between the 3D reality of the jellyfish verses the 2D simplification, as well as the rigidity of the time varying geometry imposed by the idealized model.

Notes

All figures that are submitted in color should be presented in color where possible

1 Introduction

Methods of effective locomotion must utilize and contend with both viscous and inertial forces throughout their execution. The ratio between these two forces (inertial forces divided by viscous forces) is famously known as the Reynolds number (Re). Re is often used when discussing scaling effects in fluid dynamics, as systems of the same Re are dynamically similar. Low Re flows are reversible, and a consequence of reversibility is that net fluid transport and locomotion do not occur by reciprocal motions. This result is known as the Scallop Theorem which was first introduced by [33]. One of the implications of this theorem is that scallop jet propulsion is not possible at $Re = 0$. The theorem gets its name from an idealized scallop which is shown to move forward upon contraction of its shell but then slides back to its original position upon opening its shell. Other mechanisms of reciprocal locomotion such as pectoral fin swimming in fish and flapping in stingrays are also not possible at very low Re . High Re flows, on the other hand, are dominated by pressure and inertial forces, and locomotion is possible using reciprocal motions such as flapping and undulating.

In the natural world, it appears that organisms do not use reciprocal methods of locomotion below Re of $\mathcal{O}(1)$. There are a number of ways to calculate Re , but for the purpose of the following discussion we will use the following definitions:

$$Re_m = \frac{\rho U_{ave} D}{\mu} \quad (1)$$

and

$$Re_k = \frac{\rho U_{body} D}{\mu} \quad (2)$$

where Re_m is the movement based Reynolds number, Re_k is the kinematic based Reynolds number, ρ is the density of the fluid, U_{ave} is the average forward swimming velocity, U_{body} is a characteristic speed of the swimmer with respect to itself, D is some characteristic length of the organism, and μ is the dynamic viscosity of the fluid. Flapping fins and undulatory swimming do not appear for $Re_m < 10$ [2, 5, 38]. Similar physical limits also appear to exist for jet propulsion. Both squid and octopus species hatch from the eggs already swimming at $Re_m > 10$ and grow to higher regimes (calculated from [37, 3]). Juvenile scallops use jet propulsion at $Re_m > 200$ with peak performance at $Re_m > 3000$ [24]. In jellyfish, ephyrae break off from polyps and swim at $Re_m > 1$ [17]. Ephyrae continue to grow into the mature medusae that swim at $Re_m > 100$ [21, 17]. While many studies have considered jellyfish swimming at $Re > 100$, it has yet to be studied how methods of reciprocal swimming break down as viscous forces steadily increase.

In this work, an idealized model of jellyfish swimming is used to explore the effects of Re on jet propulsion. The relatively simple design of the jellyfish bell makes it well suited for fluid-structure interaction (FSI) studies. Several research groups have previously used FSI finite difference and finite element methods to study the flows generated by hemielliptical jellyfish bells [10, 22, 40]. In these cases, the bells move with a prescribed motion so that forward velocity is an input into the system. Mosheni and Sahin [29] used a Lagrangian-Eulerian formulation to numerically solve for emergent forward motion in the jellyfish. Actual bell profiles were used as inputs into the simulations. In this paper, the immersed boundary method is used to solve the FSI problem for a two-dimensional jellyfish. Preferred contraction

and expansion kinematics are used as inputs for the simulations, but the forward motion of the jellyfish is due to the resulting fluid motion. Given the computational demands of solving the FSI problem for a wide parameter space, simplified bell shapes and kinematics in 2D flows are used so that the study is tractable. With this in mind, the purpose of this study is to explore how scale and morphology affect forward locomotion velocities in jet propulsion rather than to accurately simulate the flows generated by specific medusae.

To consider more than one form of jet propulsion, immersed boundary simulations are performed for oblate and prolate medusae and hyperexpanding ephyrae. The resulting flow structures produced by the computational medusae are then compared to those measured in actual organisms. In all cases, rhythmic contractions drive the fluid out of the bell and simultaneously move the animal forward. Depending upon the shape of the bell, the swimming mechanism can be classified as either rowing or true jet propulsion. The rowing or paddling mode is found in oblate medusae such as *Aurelia aurita* [12]. A paddling-type mechanism of swimming is also used by the ephyrae. Although the ephyral form is a discontinuous surface with deep clefts, viscous effects prevent flow between the lappets and create a hydrodynamically continuous surface [30, 17]. As a result, the ephyrae swim with a paddling motion reminiscent of oblate medusae. Prolate hydromedusae, such as *Nemopsis bachei* [11], are described as using true jet propulsion. For each body form, work put into the system and average swimming velocities are calculated for a collection of Re_k ranging from 1 to 320. For the remainder of the paper, Re will refer to Re_k .

2 Methods

2.1 Simplified Jellyfish Model

The numerical simulations are constructed such that a 2D plane cuts through the axis of symmetry of the jellyfish, generating a cross section of the bell with maximum diameter. This cross section is then modeled as an ellipse which is erased below some lower bound. The idea of approximating a jellyfish as a hemiellipsoid, while an idealization, has been used by Colin and Costello [6], Daniel [14], and McHenry and Jed [25]. The additional degree of freedom of cutting the ellipsoid anywhere along the horizontal axis is used to better capture the geometry of the jellyfish before and after contraction.

At a given instance in time, the geometry of the bell is described using the terms $a(t)$, $b(t)$, $d(t)$, (x_c, y_c) (Figure 1). The shape is then given by

$$1 = \frac{(x - x_c)^2}{a(t)^2} + \frac{(y - y_c)^2}{b(t)^2} \text{ for } y \geq y_c - d(t) \quad (3)$$

where $a(t)$ is the half-width of the bell as a function of time, $b(t) + d(t)$ is the height of the bell as a function of time, x_c is the centerline of motion which remains fixed, and y_c is determined by the motion of the fluid. In order to obtain geometries for both the completely relaxed and contracted oblate medusae, the above parameters were estimated from Figure 5 of Dabiri *et al.* [12] using least squares. The values obtained from this analysis are listed in Table 1. The parameter values for ephyra and prolate jellyfish are found by adjusting the values from the oblate data to generate reasonable shapes.

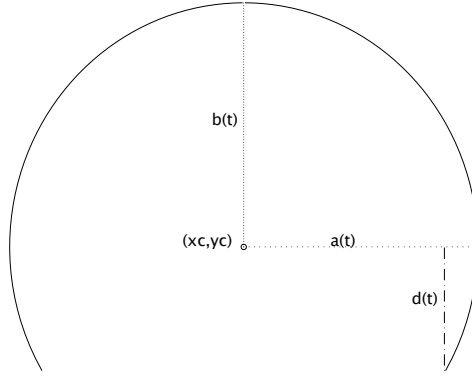


Figure 1: Diagram of the idealized jellyfish cross section. $a(t)$ gives the half width of the bell as a function of time, $b(t) + d(t)$ gives the length of the bell as a function of time, and (x_c, y_c) gives the center of the ellipse that is used to make the bell.

Parameter	a_i	b_i	d_i	d_f	p_a	p_b	p_d	t_c
Real Oblate	.051	0.0211	0.001759	-	0.3103	0.25	-3.0	.63
Ephyra	.031	-.01	0.001759	0.001758	.51	2.5	-	.63
Prolate	.05	0.075	0.025	-	.5	.2	0	2.43

Table 1: In all runs the time to refill (t_r) is three times t_c . Each run was swept over $Re = 2^n$ with $n = (0, 1, 2, 3, 4, 5, 6, 7)$ (the prolate was also run at 160 and the oblate was also run at 96, 160, 320) where the kinematic viscosity was calculated from Equations 19, 20 and 21.

To move the jellyfish bell from contracted to expanded states, time is parameterized so that $s = 0$ corresponds to a completely relaxed state, and $s = 1$ corresponds to a completely contracted state. The equations giving the values of a and b as functions of time during the contraction are defined as

$$a(s) = a_i(1 - s(p_a)) \quad (4)$$

$$b(s) = b_i(1 - s(p_b)) \quad (5)$$

where a_i is the initial half width of the bell and b_i is the initial height of the top part of the bell. For the cases of the oblate and prolate jellyfish, the equation for d is defined as

$$d(s) = d_i(1 - s(p_d)). \quad (6)$$

In the above equations, $b_i + d_i$ is the initial height of the bell, p_a is the percentage of contraction of the half width of the bell, p_b and p_d are the percentages of change in $b(s)$ and $d(s)$ respectively. The equations for the expansion kinematics are constructed similarly. s is scaled to account for the difference in contraction and expansion times by the equation

$$s = \frac{1}{2}(1 + \sin(\frac{\pi(2\tau - 1)}{2})) \quad (7)$$

where τ is the time shifted and scaled to run linearly with respect to the real time from 0 to 1. s was chosen to vary smoothly in time like a sin function, roughly approximating the velar diameters measured by Dabiri *et al.* [11]. τ is defined as

$$\tau = \frac{t - t_0}{t_c} \quad (\text{for contraction}) \quad (8)$$

$$\tau = 1 - \frac{t - t_0}{t_r} \quad (\text{for expansion}) \quad (9)$$

where t_0 is the start time of either a contraction or expansion, t_c is the time it takes to contract, and t_r is the time it takes to refill.

The time of contraction for the oblate jellyfish is set to $t_c = 0.63$ seconds, and the time of refilling was set to $t_r = 3t_c$ seconds. These numbers reflect the real time of contraction of the oblate jellyfish, *Aurelia aurita* [12]. The contraction time of the prolate jellyfish was set to $t_c = 2.43$ seconds, and time of refilling was set to $t_r = 3t_c$. This description gives the shape and horizontal position of the jellyfish at any instant in time.

Ephyral bells are not shaped like a continuous disk but rather have deep clefts between the lappets. Flow visualization studies [30, 17] suggest that there is little flow through the clefts due to viscous effects at these low Re . As a result, the surface of the ephyral bell acts as a hydrodynamically continuous surface. The ephyra are also able to hyperextend during the expansion of the bell due to the presence of the clefts. To approximate this motion, the equation for d is constructed as follows:

$$d(s) = \begin{cases} d_i((\frac{1}{p_b} - s)p_b)^3 & : s < \frac{1}{p_b} \\ d_f(\frac{p_b}{p_b - 1}(s - \frac{1}{p_b}))^3 & : s \geq \frac{1}{p_b} \end{cases} \quad (\text{for the ephyra}) \quad (10)$$

The choice of $d(s)$ was made to ensure that the body is flat when $b(s) = 0$. The times of contraction and refilling are the same as for the oblate case ($t_c = 0.63$ seconds and $t_r = 3t_c$ seconds).

2.2 Numerical Method

To solve the fluid-structure interaction problem, a two-dimensional version of the immersed boundary method is used [31]. The immersed boundary method has been applied to a wide variety of problems in biological fluid dynamics for intermediate Re including insect flight [26, 27, 28], aquatic locomotion [16, 15], and ciliary driven flows [18]. These problems typically involve a flexible structure immersed in an incompressible fluid.

The equations of motion for the two-dimensional, incompressible fluid are

$$\rho \left(\frac{\partial \mathbf{u}(\mathbf{x}, t)}{\partial t} + \mathbf{u}(\mathbf{x}, t) \cdot \nabla \mathbf{u}(\mathbf{x}, t) \right) = -\nabla p(\mathbf{x}, t) + \mu \Delta \mathbf{u}(\mathbf{x}, t) + \mathbf{F}(\mathbf{x}, t) \quad (11)$$

and

$$\nabla \cdot \mathbf{u}(\mathbf{x}, t) = 0 \quad (12)$$

where $\mathbf{u}(\mathbf{x}, t)$ is the fluid velocity, $p(\mathbf{x}, t)$ is the pressure, $\mathbf{F}(\mathbf{x}, t)$ is the force per unit area applied to the fluid by the immersed body. The independent variables are the position vector $\mathbf{x} = (x, y)$ and the time t .

The interaction between the fluid and the boundary is described by

$$\mathbf{F}(\mathbf{x}, t) = \int \mathbf{f}(r, t) \delta(\mathbf{x} - \mathbf{X}(r, t)) dr \quad (13)$$

and

$$\frac{\partial \mathbf{X}(r, t)}{\partial t} = \mathbf{U}(\mathbf{X}(r, t)) = \int \mathbf{u}(\mathbf{x}, t) \delta(\mathbf{x} - \mathbf{X}(r, t)) d\mathbf{x} \quad (14)$$

where $\mathbf{f}(r, t)$ is the force per unit length applied to the body as a function of Lagrangian position r and time t , $\delta(\mathbf{x})$ is a two-dimensional delta function, and $\mathbf{X}(r, t)$ gives the Cartesian coordinates at time t of the material point labeled by the Lagrangian parameter r . Equation 13 describes how the force is spread from the boundary to the fluid. Equation 14 evaluates the local velocity of the fluid at the boundary. In the numerical scheme the boundary is moved at the local fluid velocity at each time step which enforces the no-slip condition. Each of these equations involves a two-dimensional delta distribution δ that acts as the kernel of an integral transformation. These equations convert Lagrangian variables to Eulerian variables and *vice versa*.

The basic idea behind the implementation of the numerical method is as follows:

1. At each time step, calculate the forces the boundaries impose on the fluid. These forces are determined by the elastic spring forces connecting the boundary to the target and pairs of boundary points to each other.
2. Spread the force from the Lagrangian grid describing the position of the boundaries to the Cartesian grid used to solve the Navier-Stokes equations (equation 13).
3. Solve the Navier-Stokes equations for one time step.
4. Use the new velocity field to update the position of the boundary. The boundary is moved at the local fluid velocity, enforcing the no-slip condition (equation 14).

For the details of the exact discretization of the immersed boundary method used here, please see Peskin [32].

2.3 Discretization and Structure of the Boundary

The numerical jellyfish is designed to move forward or backwards freely along the y -axis with preferred contraction and expansion kinematics along the x -axis. In the immersed boundary method, the interface is not represented explicitly as a boundary but rather as a singular force acting on the fluid. To implement this method with preferred contraction and expansion kinematics, one must specify a singular force rather than the position of the boundary. The force required is generally not known a priori. One way to estimate this force is to compare the location of the boundary to its desired position at each time step. A force is then applied that is proportional to this difference. The error between the actual and desired motion of the boundary is then controlled by this constant of proportionality [26].

The immersed boundary is discretized so that at least two node points from the Lagrangian grid lie inside a box made from the Cartesian grid. This ensures that as the body moves through the fluid, no fluid will leak through the boundary to the other side. To discretize this particular shape we choose the parameterization:

$$(\pm a(t) \sqrt{1 - \left(\frac{((b(t) + d(t) - \epsilon) \sin(\frac{\pi r_i}{2}) - d(t))}{b(t)} \right)^2} + x_c, (b(t) + d(t) - \epsilon) \sin(\frac{\pi r_i}{2}) - d(t) + y_c) \quad (15)$$

where ϵ is taken to be a small parameter that allows for an even number of node points in the Lagrangian discretization, and r_i is a discretized version of r from equations 13 and 14 that varies from 0 to 1 ($r_i = \frac{i}{N}$ where N is the number of node points). Notice that if $a(t) = b(t)$, one would obtain an equipartitioned circle. As long as the two values are reasonably close to one another, the discretization should be close to being equipartitioned (with the final requirement of choosing ϵ intelligently). In the ephyral case the body flattens for a part of its motion; here the grid still meets the spacing requirements, however there are many more node points at the end of the body than the middle.

To prescribe contraction and expansion kinematics while allowing the bell to move forward and backward freely, the equations that describe the force the boundary applies to the fluid are distinct in x and y . For the x component, a ‘target boundary’ method is used. In the y direction, deviations from the desired shape of the bell are penalized.

For the target boundary method, a boundary that does not interact with the fluid is attached with virtual springs to the actual immersed boundary (Figures 2 and 3). The target boundary moves with the desired motion, and the springs are incorporated as a force in the x -direction that is linearly proportional to the distance between the target points and the actual points. This force is then spread to the Cartesian grid where the Navier-Stokes equations are solved.

To ensure that the bell keeps its shape during expansion and contraction, bending and stretching stiffness is enforced by connecting sets of adjacent points on the discretized Lagrangian grid with linear springs (see Figure 3). The number of node points, N , is chosen to be divisible by a set of small primes. The particular value used for these simulations was chosen to be $2^3 \times 3 \times 5 \times 7$. Given any node, it is connected in the y component to any adjacent node and to nodes that are $N/2$, $N/3$, $N/4$, $N/5$, $N/7$ and $N/8$ node points away on the Lagrangian grid. If two points that are connected move away from one another with

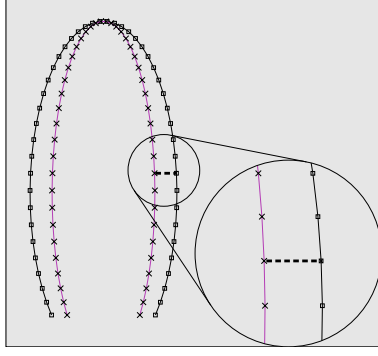


Figure 2: Diagram of the target boundary (x) and actual boundary (square). The zoomed in view shows the linear springs that connect both boundaries. In the actual simulation, springs are placed between each target and its corresponding boundary point. The distance between the two boundaries has been enlarged for clarity.

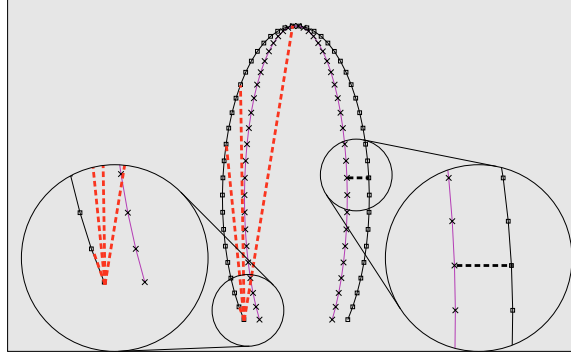


Figure 3: Diagram showing the forces used in both the x- and y-directions. The force in the y-direction is used to maintain the structure of the bell while allowing it to move freely forwards and backwards. These springs (shown by the red dashed lines) are placed between boundary points to ensure that their distances in the y-direction are preserved.

a displacement in y different from that prescribed by equation 15, a corresponding force is applied to return the distance to equilibrium. Linking the points in this way ensures that the shape of the bell is maintained while allowing the body to slide in the y direction.

Summarizing the above description leaves the following formula for $\mathbf{f}(r, t)$:

$$\begin{aligned} \mathbf{f}(r_i, t) = & k_{s_1} [\mathbf{T}(r_i, t) - \mathbf{X}(r_i, t)] \cdot e_1 \\ & + \sum_{r_j \diamond r_i} k_{s(r_j, r_i)} \text{sgn} + ((\mathbf{X}(r_j, t) - \mathbf{X}(r_i, t)) \cdot e_2) ([\mathbf{X}(r_i, t) - \mathbf{X}(r_j, t)] \\ & - [\mathbf{T}(r_i, t) - \mathbf{T}(r_j, t)]) \cdot e_2 \end{aligned} \quad (16)$$

where k_{s_1} is the spring coefficient between the target points and the immersed boundary, $r_j \diamond r_i$ means r_j is connected to r_i , $\mathbf{T}(r, t)$ describes the location of the target points, $e_1 = (1, 0)$ and $e_2 = (0, 1)$ are the standard Cartesian basis vectors, sgn returns the sign of its argument, and $k_{s(r_i, r_j)} = k_{s(r_j, r_i)}$ is the spring coefficient connecting the y components of two nodes.

Once the force on each of the Lagrangian points is determined, it is then spread to the Cartesian grid. This is done by discretizing equation 13 and using the approximation to the delta function described in [7]. Discretizing equation 13 gives

$$\mathbf{F}_{i,j} = \sum_{k=1}^N \mathbf{f}_k D_h(\mathbf{x}_{i,j} - \mathbf{X}_{r_k}) \Delta l \quad (17)$$

where $\mathbf{F}_{i,j}$ is the force on the Cartesian grid at the node labeled (i, j) , $\mathbf{f}_k = \mathbf{f}(r_k, t)$, $\mathbf{x}_{i,j}$ gives the Cartesian coordinates of the node labeled (i, j) , h is the spatial step size of the Cartesian grid, \mathbf{X}_{r_k} represents the coordinates of r_k on the Cartesian grid, and Δl is spatial step size on the Lagrangian grid approximated by $h/2$. Finally, $D_h(\mathbf{x}) = d_h(x)d_h(y)$, where $d_h(x)$ is the approximation of the delta distribution. The choice of $d_h(x)$ and is chosen to be

$$d_h(x) = \begin{cases} \frac{1}{4h}(1 + \cos(\frac{\pi x}{2h})) & , |x| \leq 2h \\ 0 & , |x| > 2h. \end{cases} \quad (18)$$

Scaling effects are studied by varying the the kinematic viscosity of the system. For this parametric study, the Re is defined (as mentioned in the introduction) so that the characteristic velocity is an input into the simulation rather than an emergent property. This Re is defined as

$$Re = Re_k = \frac{\rho l U_{body}}{\mu} = \frac{l U_{body}}{\nu} \quad (19)$$

where ν is the kinematic viscosity, U_{body} is a characteristic velocity calculated from the contraction of the bell, and l is the diameter of the jellyfish. The advantage of this formulation is that the Re is uncoupled from the forward velocity, and organisms with no net forward motion are not necessarily pulsing at $Re = 0$. U_{body} and l are given by the equations

$$l = a_i \quad (20)$$

$$U_{body} = \frac{\sqrt{(a_i p_a)^2 + (b_i p_b)^2}}{t_c}. \quad (21)$$

U_{body} gives an estimate of the average tip velocity during contraction.

In the simulations that follow, Re is varied by changing the kinematic viscosity of the fluid. We consider $Re = 2^n$ with $n = (0, 1, 2, 3, 4, 5, 6, 7)$, with the addition of $Re = 96, 160$ and 320 for the oblate case, and 160 for the prolate case.

The system of differential and integral equations given by the above equations was solved on a rectangular grid with periodic boundary conditions in both directions as described by Peskin and McQueen [32]. The velocity near the outer boundary of the domain was kept near zero on the edges of the domain by inserting four walls that were 4 grid steps away from the edges of the fluid domain. The Navier-Stokes equations were discretized on a fixed Eulerian grid. For all oblate and prolate runs the Cartesian domain was a 512×512 mesh, with the length and width scales equal to 0.25×0.25 meters. For the prolate jellyfish, the system was solved on a 512×1024 mesh with a domain width and height of 0.5×1 meters, with the exception of the faster cases where the mesh was changed to 512×1536 meters and 0.5×1.5 meters ($Re = 64, 128$) to accommodate for the extra distance traveled. For the prolate case of $Re = 160$ the length scales were still 0.5×1.5 meters but the grid size was doubled. For this last case the number of Lagrangian points was also doubled.

3 Results

3.1 Comparing locomotion and flow with Reynolds number

Figure 4 shows the resulting average forward velocities for the oblate and prolate medusae and the ephyrae as Re is varied. As Re approaches zero, the average forward velocity also approaches zero. This is consistent with the predictions of the Scallop Theorem that states that reciprocal methods of locomotion will not work in Stokes flow ($Re \approx 0$) [33]. In all cases, there is a significant decrease in forward velocity for $Re < 20$. For $Re > 100$, the average forward velocity begins to plateau. Movies of the simulations for prolate and oblate medusae and ephyra over a range of Re are presented in the supplemental materials. For $Re < 30$, vortices are not shed from the bell margins for any of the morphologies. Vorticity quickly dissipates, especially for lower Re . For prolate jellyfish at $Re > 30$, vortices separate from the bell margin and are swept downstream, forming wakes similar to those seen in [11]. For oblate jellyfish at $Re > 30$, vortices are also shed from the bell margin but circulate within and around the bell.

It is interesting to note that there is a range of Re in which decreasing viscosity actually decreases average forward velocity for the oblate jellyfish. This effect appears at Re between 16 and 96. In the the graph for the ephyra a similar effect is seen, however it is not clear whether or not the function ever truly decreases. To explain this dip, we examine the differences in flow for this range of Re . Figure 5 shows the vorticity patterns for Re 32, 64, and 96. In all cases the vortices generated by bell expansion travel back inside the bell. This behavior becomes more exaggerated as Re increases. Higher Re simulations show stronger and longer lasting vortices. Much of the vorticity is pulled into the bell, and this effect grows with Re . Furthermore, as Re increases the shed vortex strength that travels down stream also increases. We propose that it is the interaction of the starting and stopping vortices (generated during contraction and expansion) that leads to this dip in forward velocity.

To evaluate the amount of work necessary to generate the contraction and expansion kinematics, the total work done, W , was calculated as

$$W = \sum_{i=1}^T \sum_{r=1}^N \mathbf{f}_{r,i} \Delta l dx_{r,i} \quad (22)$$

where $\mathbf{f}_{r,i}$ is the force per unit length at discrete time i and Lagrangian boundary point r , and $dx_{r,i}$ is the distance traveled by the boundary point r at time i .

The total work done over four cycles is plotted in Figure 6 as functions of Re for the ephyra, oblate, and prolate medusae. Note that the work put into the pulsations locally peaks in all cases as the Re approaches 1. For the oblate and ephyra cases, the work decreases as the Re increases to 40 for the oblate jellyfish and to 10 for the ephyra. Above these values, the total work done slowly increases with Re . For the oblate case we see a dip in work as viscosity continues to decay for $Re = 320$. For the prolate jellyfish, the total work is minimized at $Re = 4$; it then rapidly increases until $Re = 32$, and finally plateaus with only small deviations until there is a large jump at $Re = 160$. Given the fact that forward velocity is also very low for $Re < 10$, paddling and jet propulsion do not appear to be particularly effective mechanisms of locomotion in this range.

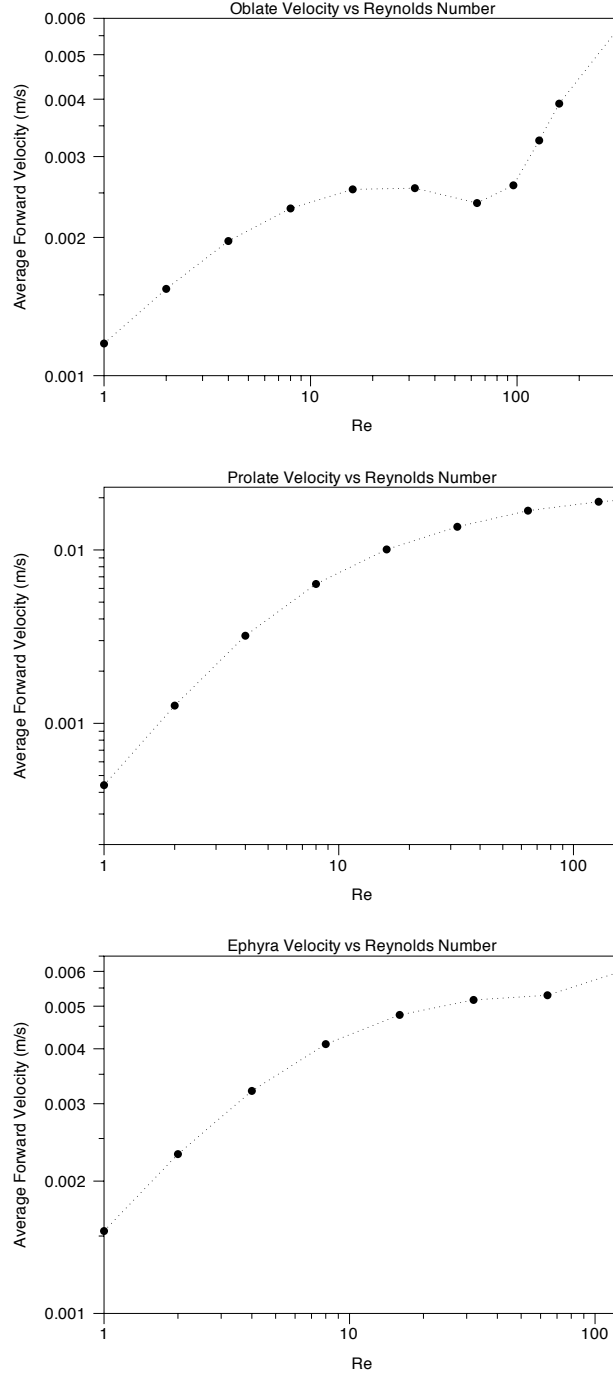


Figure 4: Average forward velocity as a function of Re for the oblate and prolate medusae and ephyra.

3.2 Forward Velocity for Different Bell Shapes

The forward velocities as functions of time for the oblate and prolate medusae and ephyral cases are shown in Figure 7 at $Re = 160, 64$ and 32 respectively. These values are chosen

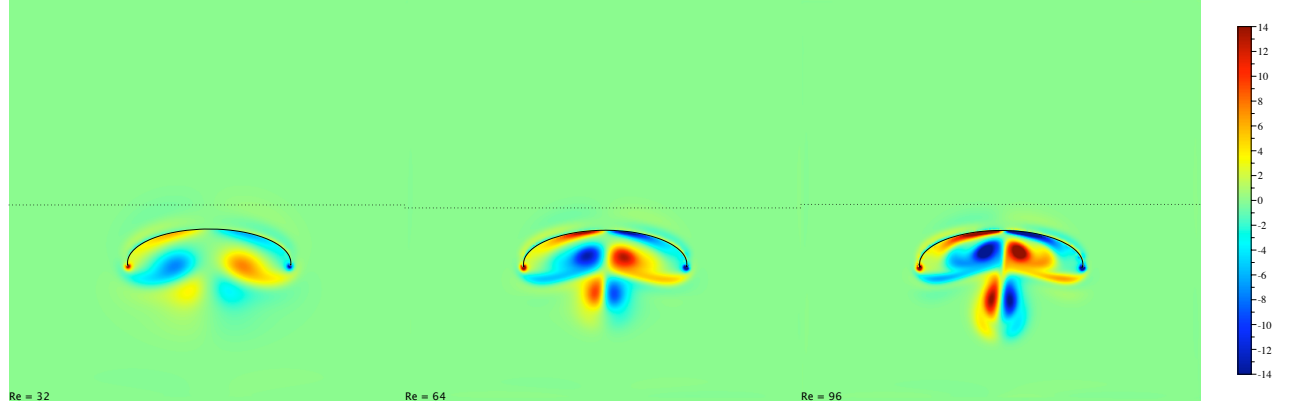


Figure 5: The end of the second expansion is shown for the oblate jelly of Re 32, 64, and 96. The dotted lines show how far the medusae will travel after four full pulsing cycles.

because they are representative of biological values (see section 4.2 below). The jellyfish moves backward during the refilling phases in ephyral cases, and moves backwards in the oblate case during the first three refilling phases. This can be seen by the fact that the velocity becomes negative toward the end of expansion. In all cases, the jellyfish shows significant slowing during expansion.

To gain insight into the flow structure causing the results of Figure 7, time sequences of vorticity generated during contraction for the oblate medusa at $Re = 160$ are presented in Figure 8. Frames 4-8 show that the two shed vortices generated by contraction are only propelled gently downstream and are primarily propelled toward the center line of the body. Frame 8 demonstrates that the generated vortices of the first contraction are pushed less than two full body lengths away from the jellyfish after nearly two full contractions. Furthermore, the two vortices formed in the first refilling phase are sucked entirely into the body, preventing another significant source of momentum from being advected downstream. The vortices that are formed during expansion are significantly deformed by the lingering contraction vortices. By the end of the second expansion the newly formed expansion vortices are in a similar position to those formed after the first expansion, and similarly will be largely sucked back into the body after the third contraction (see the supplementary material online).

Vorticity plots for the prolate case at $Re = 64$ are given in Figure 9 and show the motion over the second pulsing cycle. The vortices that have formed after the first contraction demonstrate the strong advection of vorticity downstream. The location of the vortices generated by expansion have been sucked back into the body, however they are largely expelled upon contraction (slides 1-3). Furthermore, we note that the vortices generated via contraction have shed well before the end of the contraction cycle. Note that in frames 5, 6 and 7, the closer set of shed vortices contain both the vortices formed by contraction and those generated by expansion. Figure 10 shows vorticity plots of the swimming prolate jellyfish after four contractions for $Re = 4, 8, 16$, and 32. Vorticity in the wake of the jellyfish quickly dissipates for lower Re . In addition, the separation between the body and the generated vortices decreases with Re .

Figure 11 shows vorticity plots for a time sequence of ephyral pulsing at $Re = 32$. The

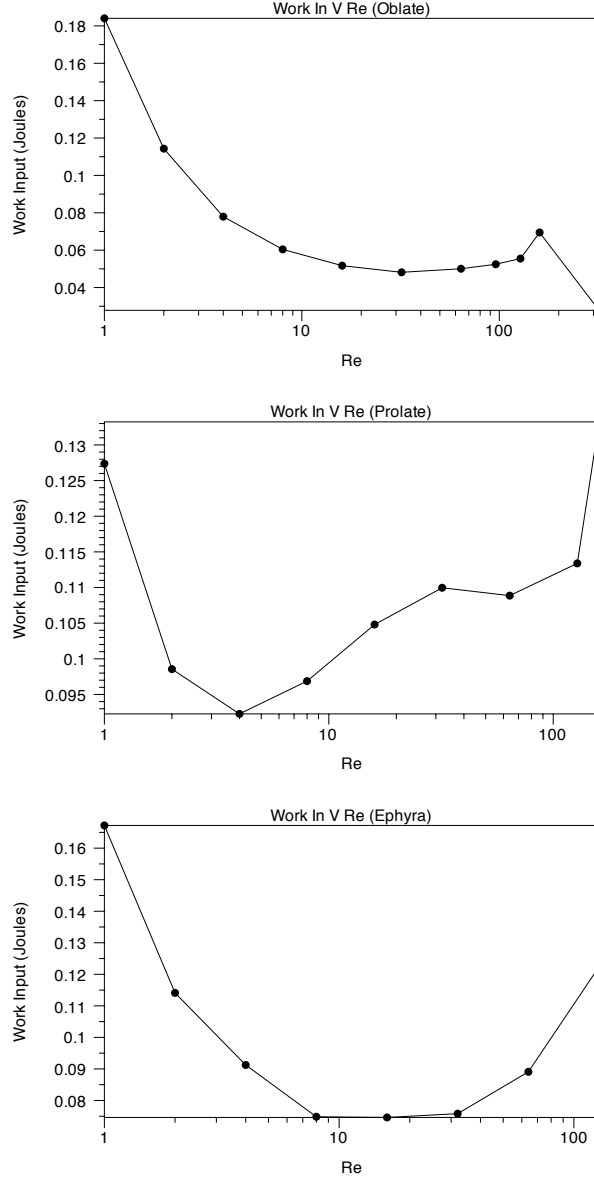


Figure 6: Total work done during four pulsing cycles for oblate jellyfish, ephyra, and prolate jellyfish as a function of Re .

model ephyra displays an inability to shed vortices in a manner that effectively produces forward motion. This is easiest to see during refilling (frames 6,7,8) when the jellyfish moves backwards toward the end of expansion. The pair of vortices that form at the bell margin during contraction do not maintain a concentrated core and are not advected downstream. Furthermore the vortices formed in earlier contractions and expansions have deteriorated significantly.

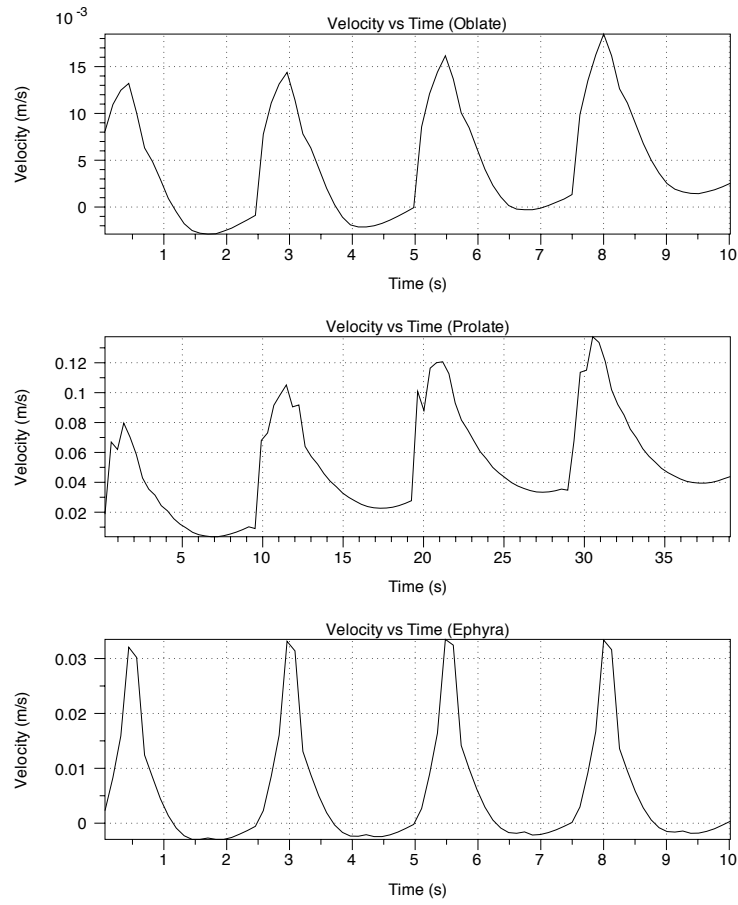


Figure 7: Forward velocity as a function of time for the oblate, prolate and ephyra over four pulsing cycles ($Re = 160, 64, 32$ respectively). Note that the velocities become negative for the cases of the oblate medusa and the ephyra. After the first cycle, prolate medusa maintain continuous forward velocities.

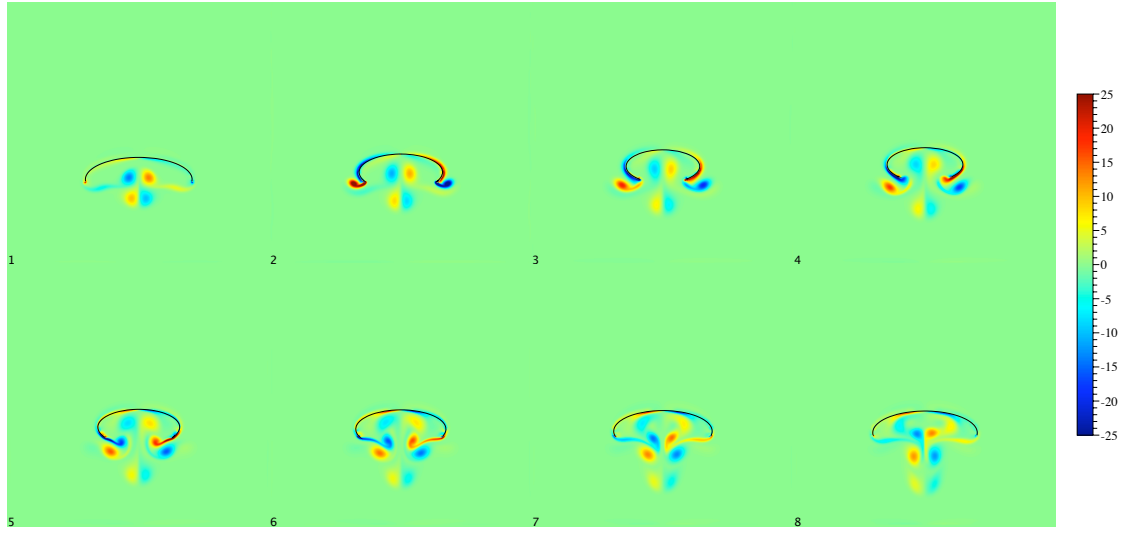


Figure 8: Vorticity plots of the fluid motion around an oblate jellyfish at $Re = 160$ during the second contraction. The vorticity has units of $seconds^{-1}$. Positive vorticity denotes clockwise motion while negative vorticity denotes counterclockwise motion. Frames 1-3 show the full contraction phase, and frames 4-8 show the refilling or expansion phase (at 16, 33, 50, 66, and 83 percent of the time taken to expand). Note that the bell is fully expanded in frame 1 and fully contracted in frame 3. The vorticity patterns found in frame 1 are due to the previous contraction.

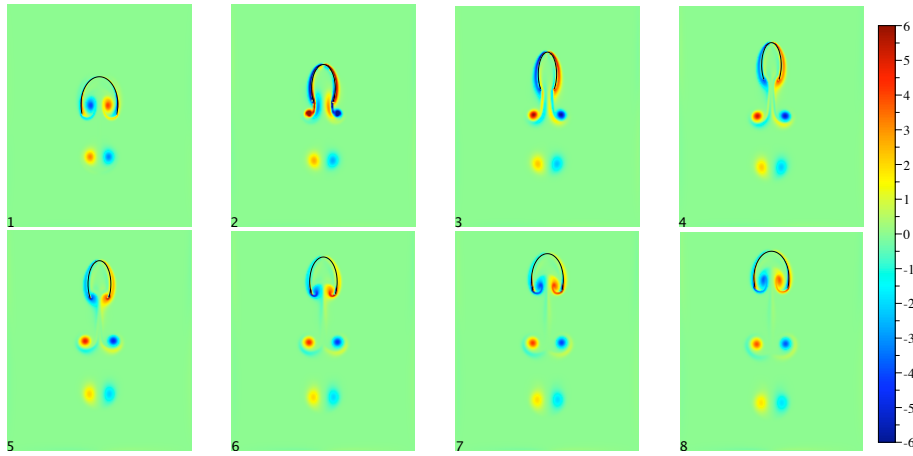


Figure 9: Vorticity plots of the fluid motion around a prolate jellyfish at $Re = 64$ during the second contraction. The vorticity has units of $seconds^{-1}$. Positive vorticity denotes clockwise motion while negative vorticity denotes counterclockwise motion. Frames 1-3 show the full contraction phase, and frames 4-8 show the refilling or expansion phase (at 16, 33, 50, 66, and 83 percent of the time taken to expand). Note that the bell is fully expanded in frame 1 and fully contracted in frame 3. The vorticity patterns found in frame 1 are due to the previous contraction.

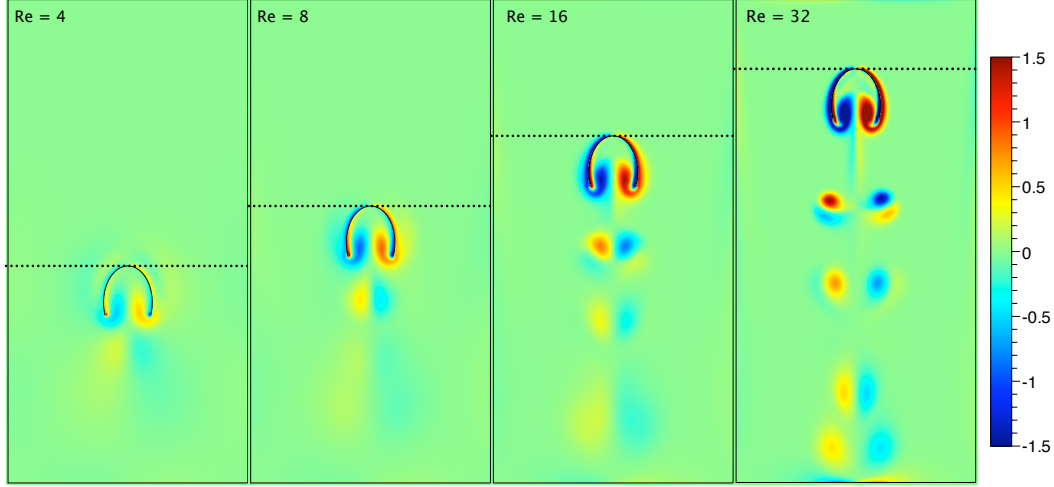


Figure 10: Vorticity plots of the fluid motion around an prolate jellyfish at $Re = 4, 16, 32, 64$. The vorticity has units of $seconds^{-1}$. Positive vorticity denotes clockwise motion while negative vorticity denotes counterclockwise motion.

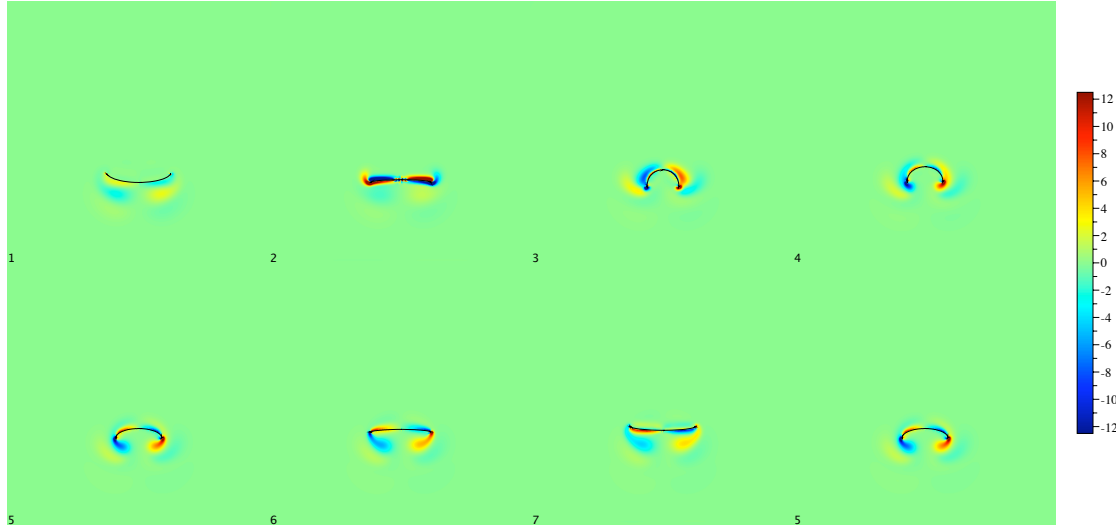


Figure 11: Vorticity plots of the fluid motion around an ephyra at $Re = 32$ during the second contraction. The vorticity has units of $seconds^{-1}$. Positive vorticity denotes clockwise motion while negative vorticity denotes counterclockwise motion. Frames 1-3 show the full contraction phase, and frames 4-8 show the refilling or expansion phase (at 16, 33, 50, 66, and 83 percent of the time taken to expand). Note that the bell is fully expanded in frame 1 and fully contracted in frame 3. The vorticity patterns found in frame 1 are due to the previous contraction.

4 Conclusions

4.1 Implications for Re limits of locomotion

These 2D simplified models provide us with a first approximation of how intermediate Re and geometry affect forward velocities in jet propulsion and paddling. By solving the fluid-structure interaction problem in 2D, we are able to explore a wide parameter space. This enables us to analyze the flow patterns that form under conditions within and beyond the biologically relevant range and to explore the role of mechanical constraints on propulsive mechanisms. These simulations also allow us to develop insights on how the jellyfish might use flow patterns to enhance motion and how these patterns break down with increasing viscosity.

The numerical results in this paper show that the average forward velocities for idealized oblate and prolate medusae and ephyrae quickly approaches zero for $Re < 10$. This corresponds to the lower Re limit observed for medusae [20], juvenile squid [37], and octopods [3]. An examination of the vorticity plots shows that for $Re < 30$, vortices do not separate from the bell margins, are not advected downstream, and as a consequence reduce the average forward velocity of the jellyfish. For $Re < 4$, vorticity quickly dissipates at the end of each contraction and expansion of the bell margin. We also find the counter intuitive result that motion can be temporarily impeded as viscosity decreases despite having over all trends of enhanced locomotion.

This work supports the idea that the behavior of intermediate Re flows sets physical limits to the types of animals observed in nature. In addition to jet propulsion, Childress and Dudley [5] suggest that below a critical Re , flapping appendages can no longer generate enough thrust to swim or fly efficiently. Alben and Shelley [2] connect this transition to a change in the behavior of the vortex wake behind the flapping plate or appendage. The fluid field loses symmetry when vortices formed behind the plate are alternately shed from each side. These vortical structures push the body into motion. Through a similar mechanism, flapping flight does not occur for $Re < 5$ [26]. This is likely a result of the fact that flapping performance (defined as the ratio of lift to drag) drastically decreases for $Re < 10$ [28]. This drop in performance can also be connected to the behavior of vortex wake. For these low Re , leading and trailing edge vortices are diffuse and do not separate from the wings. Similar vortex dynamics are observed around the bell margins for the lower Re cases with low swimming velocities.

Intermediate Re flows also define an upper limit to ciliary and flagellar locomotion. Below some critical Re , animals switch from reciprocal methods of locomotion to ciliary and flagellar locomotion. In a very interesting case, Childress and Dudley [5] describe how the Antarctic pteropod uses ciliary locomotion at low speeds and flapping locomotion at high speeds. Boletzky [36] describes how juvenile squid use cilia to propel themselves out of the viscous egg sac and use jet propulsion once they are free in the water. Similarly, many filter feeders use jet propulsion and undulation to generate large scale feeding currents and use cilia to drive small scale flows near the filtering structures and mouths [35, 19].

Species	age	diameter(m)	Re_k
<i>Aurelia aurita</i>	newly budded	0.0036	16-45
<i>Aurelia aurita</i>	smaller mature	0.036	160
<i>Aurelia aurita</i>	large mature	0.102	1286
<i>Nemopsis bachei</i>	mature	0.007	62

Table 2: Estimates of Re_k using the bell diameter and average bell tip velocity during contraction.

4.2 Comparisons to jellyfish

To compare the presented model with the jellyfish found in nature, we estimate Re_k values of real jellyfish found in nature and the results are summarized in table 2. The presented values for the oblate case representing a large *Aurelia* yield $Re = 1286$ (taking the kinematic viscosity of sea water to be $\nu = 1.05 \times 10^{-6} \text{m}^2\text{s}^{-1}$ [4]). The smaller mature oblate case in Dabiri *et al.* [12] is cited as having diameter of 3.6 cm with similar kinematics. Scaling the lengths appropriately and keeping the same contraction time and percent changes yields a Reynolds number of 160. For the prolate case we estimate Re by taking $a_i = .0035$ m, $b_i = .004$ m, $p_a = .75$, $p_b = .1$, and $t_c = .15$ s which gives $Re = 59$ [11]. Finally for the ephyral case we acknowledge that the role of b_i and p_b play a dominant role in the Re calculation, but careful measurements of ephyral bell kinematics have not been reported in the literature. To determine the range of Re for a range of ephyrae, we estimate the upper bound of Re by replacing U_{body} with the maximum tip velocity found in Feitl [17], which is 25mm s^{-1} , and take a lower bound by setting $p_b = 0$. Estimating $a_i = .18$ cm, $p_a = .5$, and $t_c = .1$ s [17], we find that a reasonable range of Re for the ephyrae is between 16 and 45. With these estimates we choose the corresponding closest Re from our simulations and compare it to the swimming dynamics of ephyrae.

After two contractions, the oblate jellyfish at $Re = 160$ moves 80 percent of its body length per contraction. This is comparable to steady state swimming velocities measured for *Aurelia* that move a little over a body length per contraction [8, 13]. Note, however, that the oblate model does not move as far as smaller mature *Aurelia aurita* from rest; the model moves only two body lengths over four contractions. To understand the differences in performance between the real and model oblate jellyfish, we examine the vortex dynamics. Dabiri *et al.* [12] describe how the starting vortex ring generated during contraction and the stopping vortex generated during expansion separate from the bell margin and travel away from the bell together. This pair of starting and stopping vortex rings form a lateral vortex superstructure (see Figure 12A,B). Adjacent lateral vortex superstructures then pull fluid into the wake and downstream of the jellyfish, enhancing forward propulsion. In contrast to this structure, the starting and stopping vortices generated by the model jellyfish are pulled back into the body, even during the final contraction when the jellyfish is moving the fastest (see the supplemental material). Furthermore, the vortices generated by the contraction of the model oblate jellyfish collapse toward the centerline, unlike the vortex dynamics observed in actual *Aurelia* [13]. For certain parameter values, the model oblate jellyfish moves with negative velocity during the expansion phase. This phenomenon has been experimentally verified in many oblate species such as *Mitrocoma cellularia* [6], *Cyanea capillata* [9], and

Aurelia aurita [8].

The differences between the vortex dynamics of the oblate model and the real jellyfish may originate from a combination of 2D effects and from the kinematic stiffness that is imposed. The 2D simulations imply that the generated vortices act as rigid cylinders whose cross sections translate within the 2D plane. Once shed during the contraction phase, it is expected that the vortices will move at the local fluid velocity in the 2D plane with no vortex stretching [1]. In the 3D case however, one vortex ring is generated during each contraction and each expansion. In order for the vorticity to move toward the centerline, the single ring would have to shrink with vorticity concentrated in a small volume. In reality, the vortex rings generated by oblate jellyfish stretch rather than shrink. The ability of the vortices to remain a short distance from the bell margin may play a crucial role in the complex starting and stopping vortex interactions found in [12]. It is reasonable to suppose that if the vortices were not pulled into the centerline then the generated stopping (expansion) vortex would help push both rings downstream. In the 2D case, the momentum of the starting (contraction) vortices pushes the stopping vortices back into the bell. The model also employs a stiff paddling motion of the lower bell which appears to sweep the vortex structures generated during expansion inside the bell. In contrast, the actual jellyfish has flexible tissue called the vellum which may allow for the vortex structures to advect downstream rather than becoming trapped inside the bell.

In the case of the prolate medusae, such as *Nemopsis bachei*, a single vortex ring is generated during the contraction that is quickly swept downstream [11] (see Figure 12C). The complicated vortex superstructures consisting of oppositely spinning starting and stopping vortices observed in oblate medusae are not present for the prolate species. We find the same pattern of vortex formation and separation for the model prolate jellyfish and, in both cases, vortices generated via contraction have shed before the end of the contraction cycle. Due to the conservation of total vorticity [39], oppositely signed vorticity is generated during bell expansion, but coherent stopping vortex structures do not form. It appears that the 2D approximation does a reasonable job of capturing the vortex dynamics for the prolate jellyfish. This may be aided by the fact that complicated 3D interactions between starting and stopping vortex rings do not need to be resolved to obtain reasonable dynamics. In the simulations, the prolate at Re of 32 and higher move between five and eight body lengths in four contractions after starting from rest, which is similar to what is observed by Dabiri [11]. For $Re = 64$, the model prolate moves roughly six body lengths over four contractions which is slightly larger than what is observed in *N. bachei*. We note however that the model prolate is a slender body without the appendages and body girth found in nature that would introduce added drag.

As for the ephyral case, we note that to our knowledge particle image velocimetry (PIV) studies have not yet been carried out on the living organism for quantitative comparison. Feitl *et al.* [17] visualized the flow around free swimming ephyrae. They note that predominance of viscous forces and describe how circulating vortices are not created in the wake. This is similar to the results found in this study for lower Re . Similarly, there have not been rigorous visualizations of vortex formation and shedding for ephyra. Nawroth *et al.* [30] found that the ephyrae of *Aurelia aurita* travel 0.5 - 1 body length per pulsation cycle, which is higher than the swimming speeds measured for the model ephyrae. It seems likely that 3D effects as well as the complex structure of the bell play a role in swimming

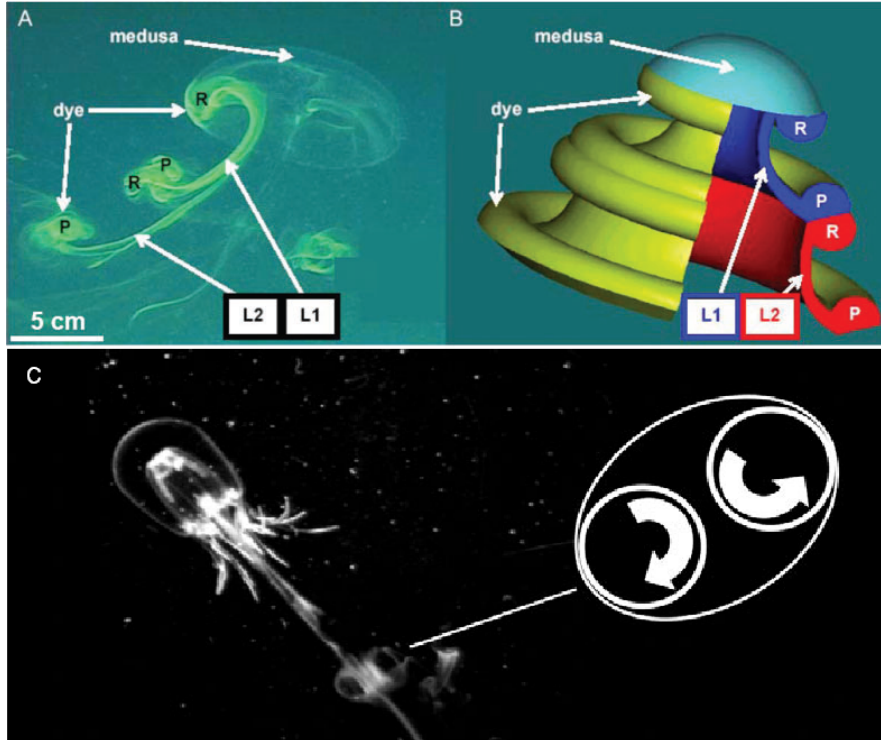


Figure 12: (A) Flow visualization of the wake of the oblate moon jellyfish *Aurelia aurita* from Dabiri *et al* [12]. (B) Corresponding schematic diagram of the vortex wake. P shows the vortex ring formed during contraction, R shows the vortex ring generated during bell expansion, and L1/L2 are label for the adjacent lateral vortex superstructures. (C) Flow visualization of vortex formation in the prolate jellyfish *N. bachei* from Dabiri *et al.* [11]. The starting vortex generated during contraction is rapidly swept downstream of the jellyfish.

performance for the juvenile jellyfish.

4.3 Limitations and future work

The goal of this study was to explore the performance of simplified organisms using jet propulsion over a range of intermediate Re . Two-dimensional simulations of jetting modeled by time varying deformations of a hemiellipsoid allow a large parameter space of shapes, kinematics, and Re to be explored. These simulations clearly show a sharp drop off in swimming performance as Re decrease below about 10, but note that the work here is not a substitute for the careful modeling of specific animals such as the work of [29, 34, 23]. The simplified model matches well with body lengths traveled per contraction and qualitatively with the prolate case but does not capture the complex vortex dynamics observed in oblate jellyfish. Future work to improve the model for a targeted study could be made by adding flexibility to the jellyfish, incorporating three-dimensional effects with an axisymmetric solver, carefully modeling the morphology and contraction kinematics for a specific species of jellyfish, etc.

It is also worthwhile to note that simulations using Peskin’s standard immersed boundary method [31] to resolve the shedding of vortex structures off these sharp boundaries for $Re > 1000$ requires spatial grid sizes that are prohibitively small. As such the authors were not able to explore the full range of Re for which organisms that use jet propulsion live. Alternative methods that better handle sharp boundaries at higher Re would be valuable for exploring the dynamics of jet propulsion at these larger scales.

5 Acknowledgements

We would like to thank Christina Hamlet, Terry Campbell, William Kier, Ty Hedrick, and Arvind Santhanakrishnan for their advice and insights throughout this research project. This work was partially funded by the Burroughs Wellcome Fund (BWF CASI ID# 1005782.01) and by the National Science Foundation (NSF FRG #0854961).

References

- [1] D. H. Acheson. *Elementary Fluid Dynamics*. University Press, Oxford, 1990.
- [2] S. Alben and M. Shelley. Coherent locomotion as an attracting state for a free flapping body. *PNAS*, 102(32):11163–11166, 2005.
- [3] S. V. Boletsky, M. Fuentes, and N. Offner. First recording of spawning and embryonic development in *Octopus macropus* (Mollusca:Cephalopoda). *Journal of Marine Biological Association of the UK*, 81:703–704, 2001.
- [4] E. Bullard. Physical properties of sea water 2.7.9, August 2010. http://www.kayelaby.npl.co.uk/general_physics/2_7/2_7_9.html.
- [5] S. Childress and R. Dudley. Transition from ciliary to flapping mode in a swimming mollusc: Flapping as a bifurcation in Re . *J. Fluid Mech.*, 498:257–288, 2004.

- [6] S. P. Colin and J. H. Costello. Morphology, swimming performance and propulsive mode of six co-occurring hydromedusae. *Journal of Experimental Biology*, 205:427–437, 2002.
- [7] R. Cortez and M. Minion. The blob projection method for immersed boundary problems. *Journal of Computational Physics*, 161:428–453, 2000.
- [8] J. H. Costello and S. P. Colin. Morphology, fluid motion and predation by the scyphomedusa *Aurelia aurita*. *Marine Biology*, 121:327–334, 1994.
- [9] J. H. Costello and S. P. Colin. Flow and feeding by swimming scyphomedusae. *Marine Biology*, 124:399–406, 1995.
- [10] O. M. Curet, I. A. Ali, N. A. Patankar, and M. A. MacIver. Fully resolved simulation of self-propulsion of aquatic organisms. In *61st American Physical Society Meeting of the Division of Fluid Dynamics*, San Antonio, TX, 2008.
- [11] J. O. Dabiri, S. P. Colin, and J. H. Costello. Fast-swimming hydromedusae exploit velar kinematics to form an optimal vortex wake. *Journal of Experimental Biology*, 209:2025–2033, 2006.
- [12] J. O. Dabiri, S. P. Colin, J. H. Costello, and M. Gharib. Flow patterns generated by oblate medusa jellyfish: field measurements and laboratory analyses. *Journal of Experimental Biology*, 208:1257–1265, 2005.
- [13] J. O. Dabiri, M. Gharib, S. P. Colin, and J. H. Costello. Vortex motion in the ocean: In situ visualization of jellyfish swimming and feeding flows, 2009. APS Div. of Flu. Dyn.
- [14] T. L. Daniel. Cost of locomotion: Unsteady medusan swimming. *Journal of Experimental Biology*, 199:149–164, 1985.
- [15] L. J. Fauci and A. L. Fogelson. Truncated newton methods and the modeling of complex immersed elastic structures. *Comm. Pure Appl. Math.*, 46:787–818, 1993.
- [16] L.J. Fauci and C. S. Peskin. A computational model of aquatic animal locomotion. *J. Comput. Phys.*, 77:85–108, 1988.
- [17] K.E. Feitl, A. F. Millett, S. P. Colin, J. O. Dabiri, and J. H. Costello. Functional morphology and fluid interactions during early development of the scyphomedusa *Aurelia aurita*. *Biol. Bull.*, 217:283291, 2009.
- [18] D. Grunbaum, D. Eyre, and A. Fogelson. Functional geometry of ciliated tentacular arrays in active suspension feeders. *J. Exp. Biol.*, 201:2575–2589, 1998.
- [19] S. H. D. Haddock. Comparative feeding behavior of planktonic ctenophores. *Integrative and Comparative Biology*, pages 1–7, 2007.
- [20] C. W. Hargitt and G. T. Hargitt. Studies in the development of scyphomedusae. *Journal of Morphology*, 21:217–262, 1910.

- [21] J. E. Higgins, M. D. Ford, and J. H. Costello. Transitions in morphology, nematocyst distribution, fluid motions, and prey capture during development of the scyphomedusa *Cyanea capillata*. *Biol. Bull.*, 214:29–41, 2008.
- [22] W.-X. Huang and H. J. Sung. An immersed boundary method for fluid-flexible structure interaction. *Computer Methods in Applied Mechanics and Engineering*, 198:2650–2661, 2009.
- [23] D. Lipinski and K. Mohseni. Flow structures and fluid transport for the Hydromedusa *Sarsia Tubulosa* and *Aequorea victoria*. *J. Exp. Biology*, 212:2436–2447, 2009.
- [24] J. L. Manuel and M. J. Dadswell. Swimming of juvenile sea scallops, *Placopecten magellanicus* (Gmelin): a minimum size for effective swimming? *J. Exp. Mar. Biol. Ecol.*, 174:137–175, 1993.
- [25] M. J. McHenry and J. Jed. The ontogenetic scaling of hydrodynamics and swimming performance in jellyfish (*Aurelia aurita*). *Journal of Experimental Biology*, 206:4125–4137, 2003.
- [26] L. A. Miller and C. S. Peskin. When vortices stick: An aerodynamic transition in tiny insect flight. *J. Exp. Biol.*, pages 3073–3088, 2004.
- [27] L. A. Miller and C. S. Peskin. A computational fluid dynamics study of clap and fling in the smallest insects. *J. Exp. Biol.*, 208:195–212, 2005.
- [28] L. A. Miller and C. S. Peskin. Flexible clap and fling in tiny insect flight. *J. Exp. Biol.*, 212:3076–3090, 2009.
- [29] K. Mohseni and M. Sahin. An arbitrary Lagrangian-Eulerian formulation for the numerical simulation of flow patterns generated by the hydromedusa *Aequorea Victoria*. *Journal of Computational Physics*, 228, 2009.
- [30] J. C. Nawroth, K. E. Feitl, S. P. Colin, J. H. Costello, and J. O. Dabiri. Phenotypic plasticity in juvenile jellyfish medusae facilitates effective animal fluid interaction. *Biol. Lett.*, pages rsbl.2010.0068v1–rsbl20100068, 2010.
- [31] C. S. Peskin. The immersed boundary method. *Acta Numerica*, 11:479–517, 2002.
- [32] C. S. Peskin and D. M. McQueen. Fluid dynamics of the heart and its valves. In H. G. Othmer, F. R. Adler, M. A. Lewis, and J. C. Dallon, editors, *Case Studies in Mathematical Modeling: Ecology, Physiology, and Cell Biology*. Prentice-Hall, New Jersey, 2nd edition, 1996.
- [33] E. Purcell. Life at low reynolds number. *Am. J. Phys*, 45:3–11, 1977.
- [34] M. Sahin, K. Mohseni, and S. Colins. The numerical comparison of flow patterns and propulsive performances for the hydromedusae *Sarsia tubulosa* and *Aequorea victoria*. *J. Exp. Biology*, 212:2656–2667, 2009.

- [35] A. J. Southward. Observations on the ciliary currents of the jelly-fish *Aurelia aurita* L. *Journal of the Marine Biological Association of the United Kingdom*, 34:201–216, 1955.
- [36] S. V. Boletzky. Ciliary locomotion in squid hatching. *Cellular and Molecular Life Sciences*, 35:1051–1053, 1979.
- [37] J. T. Thompson and W. M. Kier. Ontogenetic changes in fibrous connective tissue organization in the oval squid, *Sepioteuthis lessoniana* Lesson, 1830. *Biol. Bull.*, 201:136–153, 2001.
- [38] N. Vandenberghe, J. Zhang, and S. Childress. Symmetry breaking leads to forward flapping flight. *J. Fluid Mech.*, 506:147–155, 2004.
- [39] J. C. Wu. Theory for aerodynamic force and moment in viscous flows. *AIAA J.*, 19:432–441, 1981.
- [40] H. Zhao, J. B. Freund, and R. D. Moser. A fixed-mesh method for incompressible flow-structure systems with finite solid deformations. *Journal of Computational Physics*, 227, 2008.